

Article

Enhancement of Turbulent Convective Heat Transfer using a Microparticle Multiphase Flow

Tao Wang ^{1,2,*}, Zengliang Gao ^{1,*}  and Weiya Jin ¹

¹ Institute of Process Equipment and Control Engineering, Zhejiang University of Technology, Hangzhou 310032, China; jinweiya@zjut.edu.cn

² Institute of Mechanical Engineering, Quzhou University, Quzhou 324000, China

* Correspondence: taowang@qzc.edu.cn (T.W.); zlgao@zjut.edu.cn (Z.G.)

Received: 12 February 2020; Accepted: 9 March 2020; Published: 10 March 2020



Abstract: The turbulent heat transfer enhancement of microfluid as a heat transfer medium in a tube was investigated. Within the Reynolds number ranging from 7000 to 23,000, heat transfer, friction loss and thermal performance characteristics of graphite, Al₂O₃ and CuO microfluid with the particle volume fraction of 0.25%–1.0% and particle size of 5 μm have been respectively tested. The results showed that the thermal performance of microfluids was better than water. In addition, the graphite microfluid had the best turbulent convective heat transfer effect among several microfluids. To further investigate the effect of graphite particle size on thermal performance, the heat transfer characteristics of the graphite microfluid with the size of 1 μm was also tested. The results showed that the thermal performance of the particle size of 1 μm was better than that of 5 μm. Within the investigated range, the maximum value of the thermal performance of graphite microfluid was found at a 1.0% volume fraction, a Reynolds number around 7500 and a size of 1 μm. In addition, the simulation results showed that the increase of equivalent thermal conductivity of the microfluid and the turbulent kinetic energy near the tube wall, by adding the microparticles, caused the enhancement of heat transfer; therefore, the microfluid can be potentially used to enhance turbulent convective heat transfer.

Keywords: heat transfer enhancement; multiphase flow; microfluid; Eulerian–Eulerian model

1. Introduction

The viscous layer is dominated by heat conduction, which hinders the heat transfer in a tube. It has been found that nanofluid can enhance heat transfer. Typical nanoparticles of metals, such as Al and Cu, and metal oxides such as TiO₂, Fe₃O₄, Al₂O₃ and CuO, have been used for nanofluid [1–8]. Further, nanofluids have also been used with other enhancing devices for the heat transfer process, such as wire coils, twisted tape and roughened heat exchanger surfaces [9–13]. Recently, the combination of nanofluid, inserts and roughened heat exchanger surfaces has been reported [14,15]. Although nanofluids can improve heat transfer inside a tube at a low particle volume fraction, they have some disadvantages. It is difficult to prepare nanoparticles and nanofluid suspensions, and the smaller the particles, the more serious the particle aggregation. Further, some poisonous particles are small and easily diffused into the air and inhaled by the human body [16]. In contrast, the particle size of the microparticles is large, which can alleviate such problems. Chang et al. [17] studied the characteristics of heat transfer of Al-water microfluid with swirl in a circular tube. Their results showed that the Nusselt number can be enhanced by increasing the swirl intensity or Reynolds numbers. Ghorbani et al. [18] investigated the enhancement of the laminar characteristics of convective heat transfer using microparticle suspensions with a Reynolds number ranging from 6 to 24. Their results indicated a significant enhancement of the convective heat transfer coefficient by adding the microparticles. Wang et al. [19] employed a numerical model to study the convective heat transfer of

a Cu–water microfluid. Their simulation results showed the thermal performance can be improved from 1.1 to 2.3.

This paper aims to study the turbulent convective heat transfer of Graphite, Al₂O₃ and CuO microfluids with a volume fraction of 0.25%, 0.5%, 0.75% and 1.0%, as well as a particle size of 5 µm and Reynolds numbers ranging from 7000 to 23,000. To determine the best heat transfer effect for the microfluid, the influence of particle size on thermal performance was also tested.

2. Experiments

2.1. Microfluid Preparation

Table 1 lists the properties of the purchased microparticles. Firstly, the microparticles were weighed by an electronic scale with an accuracy of 0.001 g, according to the volume fraction of the microparticles. Secondly, graphite, Al₂O₃ and CuO microparticles were added into the water, measured according to their volume fraction, and stirred evenly by a bar. Finally, the microparticle suspensions were oscillated for at least 45 min by using an ultrasonic vibrator (35 kHz, 120 W) to reduce microparticle aggregation. The filter papers of 10 µm were used to remove the big aggregated microparticles. The microparticles with a volume fraction of 0.25%, 0.5%, 0.75% and 1.0% were prepared.

Table 1. Parameters of the microparticles.

Parameter	Graphite	Al ₂ O ₃	CuO
Average grain diameter/µm	5	5	5
Purity/%	99.9	99.9	99.9
Density/kg·m ⁻³	2250	3970	6500
Specific heat/J·kg ⁻¹ ·°C ⁻¹	708	765	540
Thermal conductivity/W·m ⁻¹ ·K ⁻¹	127	25	18

For the sedimentation analysis of the microfluids, the microfluid was stirred evenly and placed into a graduated cylinder of the specified scale (100 ml). The heights of the clear liquid layer and the sedimentation layer were recorded at different periods during the standing process by visualization. The velocity of sedimentation was calculated from the relationship between the height of the clear liquid layer and time. Table 2 shows the velocity of the sedimentation calculated by the experimental data matched with that calculated by the Stokes formula [20] as shown in Equation (1), within an error of 10%.

Table 2. The velocity of sedimentation.

Material Property	Experimental Velocity /mm·s ⁻¹	Calculated Velocity by the Stokes Formula [17] /mm·s ⁻¹	Error/%
Graphite	0.021	0.0198	6
Al ₂ O ₃	0.050	0.0469	7
CuO	0.091	0.0866	5

Stokes formula:

$$V = \frac{(\rho_p - \rho_w)d_p^2 g}{18\mu_w} \quad (1)$$

2.2. Experimental Device

An experimental device was set up to study the turbulent convective heat transfer of the microfluid, which is shown in Figure 1. This device consists of two loops, i.e., a hot water loop and a cold fluid loop. A counter-flow heat exchanger was used to link the two loops. There were 4 Pt100 thermal resistance

apparatus to measure the inlet and outlet temperatures with two for the cold water flow and two for hot water flow. The Pt100 and the flowmeters were separately connected to ADAM 4015 and ADAM 4117. Hot water, pumped from the hot water tank, was heated by a 3 kW heater rod at around 320 K, then the hot water was cooled down by flowing through the shell and eventually heated back to the hot water tank. The cold microfluid from the cool water tank at around 300 K was heated by flowing through the tube; it then flowed back to the cool water tank after being cooled in the cooler. Therefore, the inlet temperatures of the hot and cold water flows were fixed in the experiments. The inner tube, with an inner diameter of 12 mm and made of copper, had a thermal conductivity of $376 \text{ W}\cdot\text{m}^{-1}\cdot\text{K}^{-1}$, while the stainless steel shell had a shell-inner diameter of 38 mm. Both of the tube and shell wall thicknesses were 2 mm. The one-meter-long test section was well insulated with wrapping glass wool inside and aluminum foil tape outside. Volume flow rates, pressures and temperatures were measured by turbine flowmeters, pressure transducer and thermal resistance (Pt100), respectively. All test data were recorded through an ADAM 4561, which converted RS485 signals to USB for use on a computer.

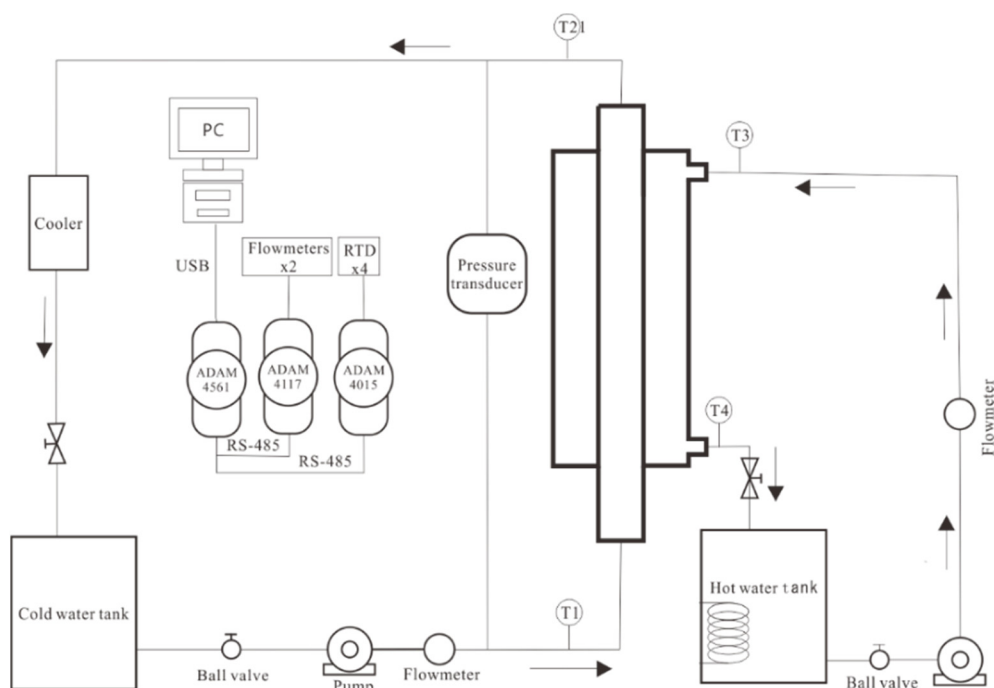


Figure 1. Experimental process.

For accurate results, the device's uncertainty was evaluated [21]. Table 3 shows the uncertainties of the experimental instruments' performance, depending on the accuracy of each instrument. Table 4 lists the uncertainties of the experimental variables. All the ranges of experimental uncertainties were less than 15%; the instruments and variables thus showed strong reliability and accuracy.

Table 3. Uncertainty of the experimental instruments.

Apparatus Name	Uncertainty /%
Pt100	0.5
pressure transducer	0.5
turbine flowmeters	0.5

Table 4. Uncertainty of the experimental parameters.

Experimental Parameters	Uncertainty /%
f	1.42
Nu	12
Re	0.55

2.3. Data Processing

2.3.1. The Thermophysical Properties of Microfluids

The physical properties used for the microfluid were calculated. The density of the microfluid was evaluated by the following;

$$\rho_{mf} = (1 - \phi)\rho_w + \phi\rho_{mp} \quad (2)$$

The specific heat of the microfluid was calculated by

$$C_{p,mf} = \frac{\phi\rho_{mp}C_{p,mp} + (1 - \phi)\rho_w C_{p,w}}{\rho_{mf}} \quad (3)$$

The thermal conductivity was evaluated by the Maxwell model [22], as follows;

$$\frac{k_{mf}}{k_w} = \frac{k_{mp} + 2k_w + 2\phi(k_{mp} - k_w)}{k_{mp} + 2k_w - \phi(k_{mp} - k_w)} \quad (4)$$

The viscosity of the microfluids was evaluated by Einstein's formula [23]

$$\mu_{mf} = \mu_w(1 + \eta\phi) \quad (5)$$

2.3.2. Heat Transfer and Friction Factor

The heat flow was calculated as follows;

$$\dot{Q}_c = C_{p,c}\rho_c\dot{V}_c(T_{c,out} - T_{c,in}) \quad (6)$$

$$\dot{Q}_h = C_{p,h}\rho_h\dot{V}_h(T_{h,out} - T_{h,in}) \quad (7)$$

It was found from the experimental results that the heat provided by the hot fluid was 5% to 8% higher than that absorbed by the cold fluid due to the heat loss caused by the convection and radiation of the test part and the surrounding environment. Considering the heat loss, the average heat transfer rate is calculated as follows;

$$\dot{Q}_{ave} = (\dot{Q}_c + \dot{Q}_h)/2 \quad (8)$$

where \dot{Q}_c is the heat flux absorbed by the cold fluid, and \dot{Q}_h is the heat flux provided by the hot fluid.

The overall heat transfer coefficient (K) can be calculated as

$$K = \dot{Q}_{ave}/A_i\Delta T_{LMTD} \quad (9)$$

where A_i is the heat transfer inner-surface area of the tube, and ΔT_{LMTD} is the logarithmic mean temperature difference.

The inside surface area of the heat transfer of the tube is calculated as follows;

$$A_i = \pi d_i L \quad (10)$$

where d_i is the inside diameter of the tube, and L is the length of the tube.

The heat transfer coefficient (h_i) was evaluated as below;

$$1/K = d_o/h_i d_i + d_o \ln(d_o/d_i)/2k + 1/h_o + R_f \quad (11)$$

where d_o is the outside diameter of the tube, k is the length of the tube, h_i is the heat transfer coefficient on the inside surface of the tube, h_o is the heat transfer coefficient on the outside surface of the tube, k is the thermal conductivity of the material of the tube, and R_f is the thermal resistance of dirt and scale.

The last three elements of Equation (11) are constant, and h_i can be expressed as Equation (12), based on the Wilson plot method [24];

$$h_i = cRe^n \quad (12)$$

where c and n are the constant.

The heat transfer coefficient can be re-expressed as

$$h_i = d_i / (1/K - b) d_o \quad (13)$$

where b is the constant.

The average Nusselt number is evaluated by

$$Nu = h_i d_i / k \quad (14)$$

where k is the heat transfer coefficient of water or microfluids.

The tube Reynolds number was evaluated as follows;

$$Re = \rho V d_i / \mu \quad (15)$$

where μ is the viscosity of water or microfluids, ρ is the density of water or microfluids, and V is the mean velocity of tube inlet.

The friction factor (f) is expressed by

$$f = 2\Delta P d_i / \rho V^2 L \quad (16)$$

where Δp is pressure loss between tube inlet and outlet.

The thermal performance factor can be calculated as

$$\eta = (Nu_{mf} / Nu_w) / (f_{mf} / f_w)^{1/3} \quad (17)$$

where Nu_{mf} and f_{mf} are the Nusselt number and friction loss of the microfluids, and Nu_w and f_w are the Nusselt number and friction loss of the water, respectively.

2.4. Experimental Results and Discussion

2.4.1. Heat Transfer and Flow Characteristics

The Nusselt number, friction factor and thermal performance at different Reynolds numbers for the graphite, Al_2O_3 and CuO with different volume fractions were calculated with experimentally measured temperatures, pressure loss values and flow rates. The Nusselt number results for three kinds of microfluids are shown in Figure 2; the Nusselt number does not only increase with Reynolds number increasing but also increases with the volume fraction of microparticle increasing. In addition, the Nusselt number of the graphite microfluid was higher than that of any other microfluid under the same conditions and was about 1.3–1.4 times, 1.5–1.7 times, 1.7–2.0 times and 2.0–2.3 times the Nusselt number of the water at a volume fraction of 0.25%, 0.5%, 0.75% and 1.0%, respectively. The reason is that the equivalent thermal conductivity of the microfluid increased according to Equation (4), due to the higher thermal conductivity of adding graphite microparticle about $127 \text{ W}\cdot\text{m}^{-1}\cdot\text{K}^{-1}$, which is more

than 200 times that of water and 5 times the thermal conductivity of Al_2O_3 , and 7 times the thermal conductivity of CuO . The Al_2O_3 microfluid was about 1.1–1.2 times, 1.2–1.4 times, 1.3–1.5 times and 1.4–1.6 times the Nusselt number of the water at volume fraction of 0.25%, 0.5%, 0.75% and 1.0%, respectively, and the CuO microfluid was about 1.1–1.2 times, 1.2–1.3 times, 1.3–1.4 times and 1.3–1.5 times the Nusselt number of the water at a volume fraction of 0.25%, 0.5%, 0.75% and 1.0%, respectively. The Nusselt numbers of the Al_2O_3 and CuO microfluids were similar because the thermal conductivity of Al_2O_3 and CuO were almost the same, and more than about 29 times the thermal conductivity of water. Therefore, the heat transfer performance could be enhanced by adding microparticles with a higher thermal conductivity than water. Further, graphite has good chemical stability, electrical conductivity and thermal conductivity, so the microfluid mixed by this particle had better heat transfer performance than Al_2O_3 and CuO .

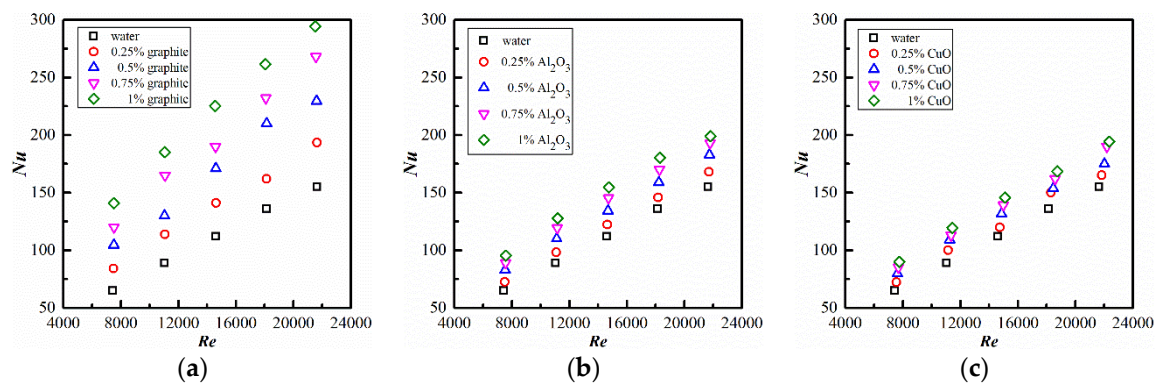


Figure 2. Variations of Nu with Re : (a) graphite; (b) Al_2O_3 ; (c) CuO .

The results of the friction factor with the Reynolds numbers are shown in Figure 3. In the tested range, the friction factors of the three kinds of microfluids were all higher than that of water. The friction factor of the graphite microfluid was 0.006–0.003, 0.008–0.005, 0.01–0.006 and 0.012–0.007 higher than that of water, the friction factor of the Al_2O_3 microfluid was 0.007–0.004, 0.01–0.006, 0.01–0.007 and 0.0144–0.008 higher than that of water, and the friction factor of the CuO microfluid was 0.009–0.008, 0.012–0.01, 0.014–0.01 and 0.016–0.011 higher than that of water at a volume fraction of 0.25%, 0.5%, 0.75% and 1.0%, respectively. The reason was that the equivalent viscosity of the microfluid increased due to the addition of microparticles according to Equation (5). The higher the volume fraction of the microparticles, the greater the equivalent viscosity of the microfluid. The friction factor of the graphite microfluid was lower than that of any other microfluid under the same conditions due to its lubrication. Generally, the friction factor decreases with Reynolds number increasing but increases with volume fraction of microparticle increasing.

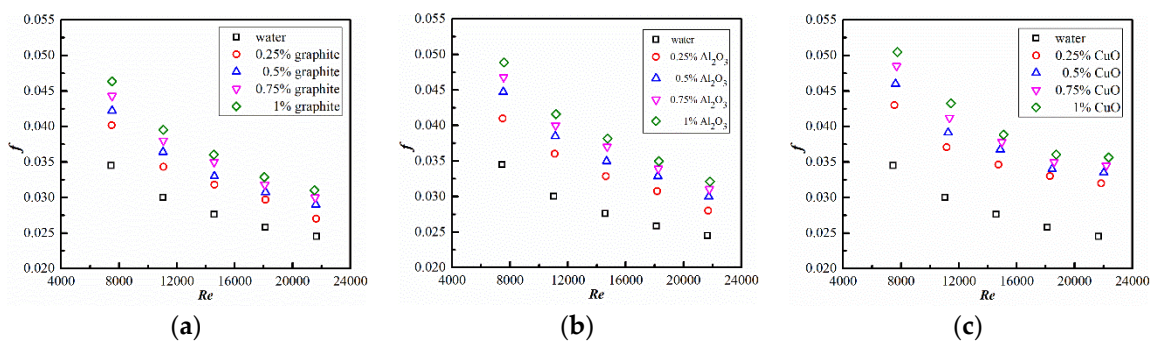


Figure 3. Variations of f with Re : (a) graphite; (b) Al_2O_3 ; (c) CuO .

2.4.2. Thermal Performance

The results of the thermal performance factor with different Reynolds numbers are shown in Figure 4; the thermal performance for all tested microfluids was greater than 1, which was better than water. Therefore, in the experimental range, it can be concluded that the positive effects of the enhanced heat transfer outweighed the negative effects of the increased friction losses. The higher the volume fraction of the microparticles, the greater the thermal performance of the microfluid. The thermal performance of the graphite microfluid was higher than that of any other microfluid under the same conditions, and the thermal performance factor was about 1.2–1.4, 1.5–1.7, 1.7–1.9 and 1.9–2.2, at a volume fraction of 0.25%, 0.5%, 0.75% and 1.0%, respectively. The thermal performance factor of the graphite microfluid was the highest, which showed the comprehensive characteristics of the heat transfer performance. Further, the friction losses of the graphite microfluid were the best among the tested microfluids. The maximum thermal performance of 2.23 was found with the graphite microfluid at a 1.0% volume fraction and a Reynolds number around 7500. As shown in Figure 4, thermal performance decreases with an increase in the Reynolds number and increases with an increasing volume fraction of microparticles.

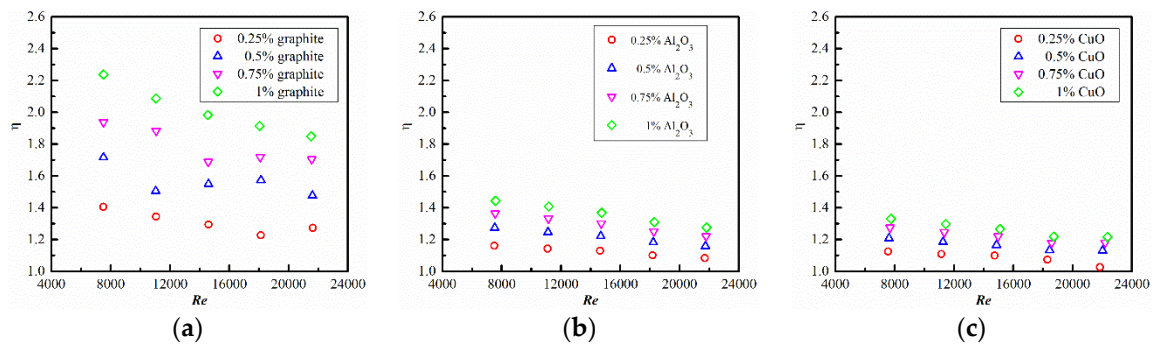


Figure 4. Variations of η with Re : (a) graphite; (b) Al_2O_3 ; (c) CuO .

2.4.3. Regression Equation

According to the obtained experimental data of the graphite microfluid and the correlative formula, comparisons between the experimental value and the predicted value for the Nusselt number and the friction factor are illustrated in Figures 5 and 6. The nonlinear curve fit equation coefficients, as shown in Equations (18) and (19), were calculated with the least square method solved by the iteration algorithm of Levenberg Marquardt. It can be observed that the predicted results are in good agreement with the experimental data within a deviation of $\pm 10\%$ for the Nusselt number and $\pm 5\%$ for the friction factor.

$$Nu = 0.0002Re^{0.7454}Pr^{3.4007}(1 + \phi)^{67.6574} \quad (18)$$

$$f = 1.0299Re^{-0.3679}(1 + \phi)^{17.6099} \quad (19)$$

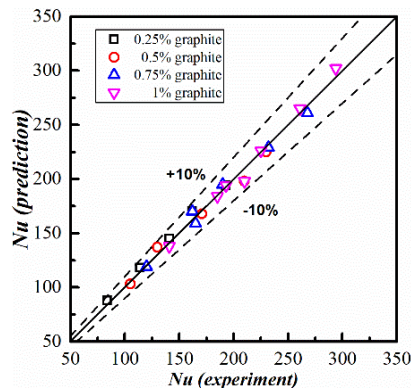


Figure 5. Comparison of Nu between the experiments and the predictions from the regression equation.

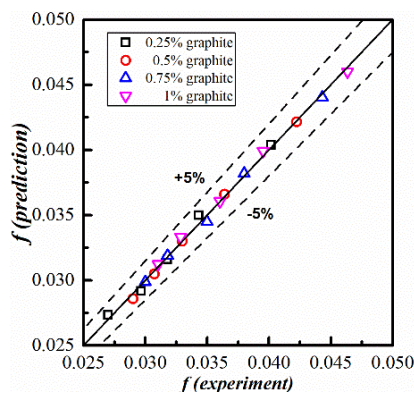


Figure 6. Comparison of f between the experiments and the predictions from the regression equation.

2.4.4. Graphite Particle Size and Regression Equation

The above results show the enhanced heat transfer of the graphite microfluid. The effect of the particle size on thermal performance is discussed in this section. The results for particle sizes of 1 μm and 5 μm are shown in Figures 7 and 8. Compared with a graphite particle size of 5 μm , the Nusselt number and friction factor for a graphite particle size of 1 μm were more than those for a size of 5 μm . The thermal performance of a graphite microfluid with a particle size of 1 μm was higher than that for a particle size of 5 μm .

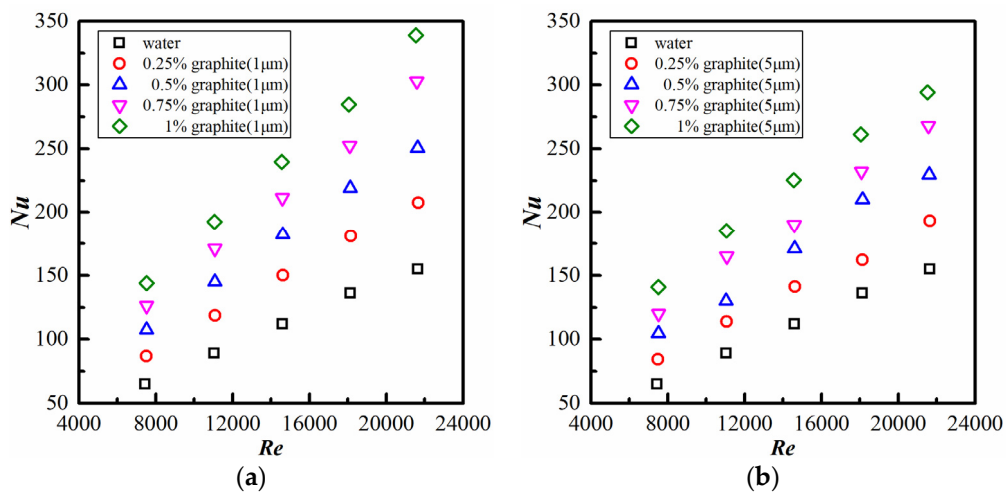


Figure 7. Relation diagram of Nu with Re : (a) a graphite particle size of 1 μm ; (b) a graphite particle size of 5 μm .

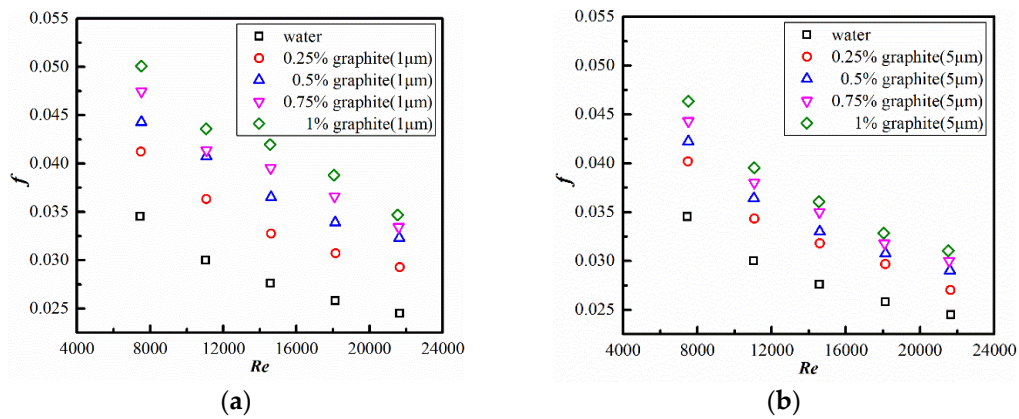


Figure 8. Relation diagram of f with Re of microparticle size: (a) a graphite particle size of $1\ \mu\text{m}$; (b) a graphite particle size of $5\ \mu\text{m}$.

Based on the obtained experimental data on particle size, comparisons between the experimental value and predicted value for different particle sizes for the Nusselt number and friction factor are shown in Figures 9 and 10. The regression equation can be expressed as in Equations (20) and (21), where $D_{ref} = 2.5\ \mu\text{m}$, and D_{mp} = the diameter of the particles in micrometers. The deviation of the correlation data from the experimental data is $\pm 10\%$ and $\pm 5\%$ for the Nusselt number and friction factor, respectively.

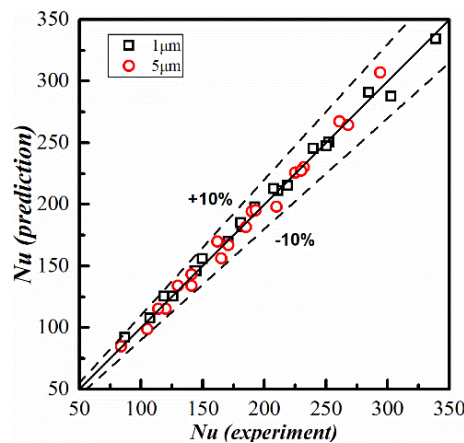


Figure 9. Comparison of Nu between the experiments and the predictions from the regression equation.

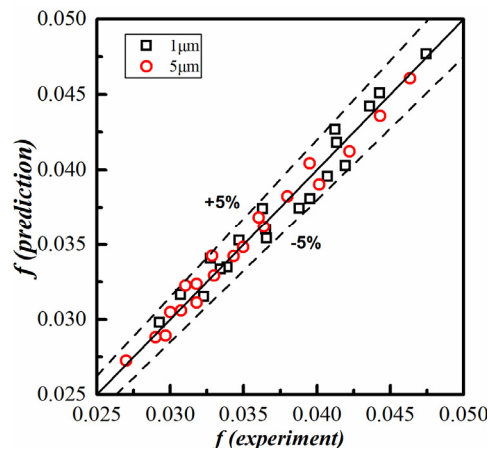


Figure 10. Comparison of f between the experiments and the predictions from the regression equation.

$$Nu = 0.0094Re^{0.7891}Pr^{1.0986}(1 + \phi)^{63.9181}\left(\frac{D_{mp}}{D_{ref}}\right)^{-0.0523} \quad (20)$$

$$f = 0.7891Re^{-0.3389}(1 + \phi)^{22.3896}\left(\frac{D_{mp}}{D_{ref}}\right)^{-0.0558} \quad (21)$$

3. Numerical Study

3.1. Simulation Model

For studying the heat transfer mechanism in detail, the heat transfer process of the microfluid flow through the tube were simulated by an Eulerian–Eulerian model using the CFD software. The details of the continuity equations given by Equation (22), the momentum conservation equation given by Equations (23) and (24), and the energy equation given by Equation (25) are shown, respectively, as follows;

$$\frac{\partial}{\partial t}(\alpha_i \rho_i) + \nabla \cdot (\alpha_i \rho_i V_i) = 0 \quad (22)$$

$$\frac{\partial}{\partial t}(\alpha_f \rho_f V_f) + \nabla \cdot (\alpha_f \rho_f V_f V_f) = -\alpha_f \nabla p + \nabla \cdot \tau_f + \alpha_f \rho_f g + K_{sf}(V_s - V_f) \quad (23)$$

$$\frac{\partial}{\partial t}(\alpha_s \rho_s V_s) + \nabla \cdot (\alpha_s \rho_s V_s V_s) = -\alpha_s \nabla p - \nabla p_s + \nabla \cdot \tau_s + \alpha_s \rho_s g + K_{sf}(V_f - V_s) \quad (24)$$

$$\frac{\partial}{\partial t}(\alpha_i \rho_i h_i) + \nabla \cdot (\alpha_i \rho_i v_i h_i) = \nabla \cdot \alpha_i k_{i,eff} \nabla T_i - h_{ij}(T_i - T_j) \quad (25)$$

In the Equations, α_i is the volume fraction of phase i , ρ_i is the density of phase i , v_i is the velocity of phase i , h_i is the specific enthalpy of phase i , g is the gravity acceleration and i represents either the fluid (f) or solid (s) phase;

$$K_{sf} = \begin{cases} \frac{18}{Re_s} \left[1 + 0.15(\alpha_f Re_s)^{0.687} \right] \frac{\alpha_s \rho_f |V_s - V_f|}{d_s} \alpha_f^{-2.65} & \alpha_f > 0.8 \\ \frac{150 \alpha_s (1 - \alpha_f) \mu_f}{\alpha_f d_s^2} + 1.75 \frac{\alpha_s \rho_f |V_s - V_f|}{d_s} & \alpha_f \leq 0.8 \end{cases} \quad (26)$$

$$\tau_i = \alpha_i \mu_i \left[\nabla V_i + (\nabla V_i)^T \right] + \alpha_i \left(\lambda_i - \frac{2}{3} \mu_i \right) (\nabla \cdot V_i) I \quad (27)$$

where K_{sf} is the interphase momentum exchange coefficient and defined by the Gidaspow model [25], which is a combination of the Wen and Yu models [26] and Ergun model [27], τ_i is the phase i stress–strain tensor shown in Equation (27), d_s is the particle diameter of solid phase and μ_i is the shear viscosity of phase i and λ_i is the bulk viscosity of phase i .

Equation (28) is the transport equation for the closure of the solid phase momentum equation

$$\frac{3}{2} \left[\frac{\partial}{\partial t}(\alpha_s \rho_s \Theta_s) + \nabla \cdot (\alpha_s \rho_s V_s \Theta_s) \right] = (-p_s I + \tau_s) : \nabla V_s + \nabla \cdot (k_{\Theta_s} \nabla \Theta_s) - \gamma_{\Theta_s} + \varphi_{fs} \quad (28)$$

where $(-p_s I + \tau_s) : \nabla v_s$ is energy generated by the solid stress tensor, $k_{\Theta_s} \nabla \Theta_s$ is the energy diffusion, Θ_s is the granular temperature of the solid phase, γ_{Θ_s} is the collisional dissipation of energy due to collisions between particles and φ_{fs} is the energy exchange between the solid phase and the fluid or solid phase.

The two-fluid model (TFM) has been successfully applied in the literature to predict the heat transfer coefficient [28,29]. The details of the computational conditions are shown in Table 5. Two-equation turbulence models ($K-\varepsilon$) are widely used to simulate the turbulent flow and heat transfer due to their robustness, economy and reasonable accuracy [30]. Bayat et al [31] found that the simulation results of applying the Realizable $K-\varepsilon$ model agreed well with the Gnielinski [32] experiment results and the test

results in this paper also agree well with the simulation results by using the Realizable $K-\epsilon$ turbulence model. A near-wall modeling method (enhanced wall treatment), combined with a two-layer model with enhanced wall functions, can be used with coarse meshes as wall-function meshes, as well as fine meshes as low-Reynolds number meshes, typically with the first near-wall node placed at $y^+ \approx 1$. Grid convergence was checked on the grid size of 0.5–2 mm and the growth ratio of the boundary layer of 1.1, 1.3 and 1.5 under the condition of $Y^+ < 1$. Through some trial simulations of the grid models, when the grid size was 1 mm and the growth ratio was 1:1, the grid size decreased and the changes of simulation results were less than 1%. The computational domain is shown in Figure 11; the thickness of the tube was 2 mm, and the details of the computational boundary conditions are shown in Table 6. SIMPLE was used to solve the pressure–velocity coupling algorithm. After solving the initial model, the velocity profiles at the outlet boundary were imposed on the inlet boundary, and the last solution was recalculated for precision. The iterative calculations were performed until the normalized residual fell below a convergence criterion (less than 10^{-6} for the energy residual and less than 10^{-4} for all other variables), and the variation of the Nusselt number, pressure loss and outlet temperature profiles were kept steady.

Table 5. Details of the computational conditions.

Fluid	Microfluid	Water
Fluid flow	Eulerian multiphase	single-phase model
Turbulence modeling	Realizable $k-\epsilon$ model	Same as microfluid
Near-wall modeling method	Enhanced wall treatment	Same as microfluid
Microfluid concentrations	0.25%, 0.5%, 0.75%, 1.0%	0%
y^+	<1	<1

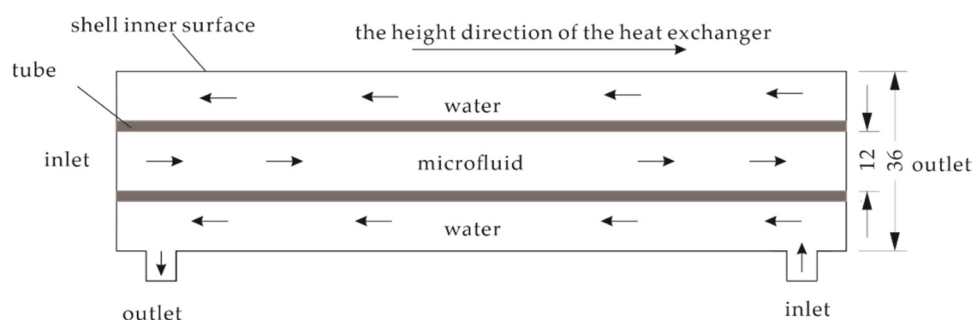


Figure 11. The computational domain.

Table 6. Details of the boundary conditions.

Boundary Conditions	Setting
tube wall	No-slip
shell wall	No-Slip
tube inlet	velocity
tube outlet	pressure
shell inlet	velocity
shell outlet	pressure
tube inlet temperature	300 K
shell inlet temperature	320 K
two sides of the tube wall	coupled thermal conditions
shell wall	adiabatic

3.2. Simulation Results and Discussion

The results of the experiment and simulation of the water and the graphite microfluid at a volume fraction of 1.0% are shown in Figure 12. The results of the simulation matched those of the experiments

within an error of 12%. The simulation results for the turbulent kinetic energy, the interphase heat transfer coefficient and the temperature of graphite particle sizes of 1 μm and 5 μm in the middle cross-section of the tube at a volume fraction of 1.0% with a flow of $Re = 23,000$ are demonstrated in Figures 13–15. As seen in Figure 13, the water-phase and the solid-phase (graphite) turbulent kinetic energy for the 1% graphite microfluid in the middle cross-section of the tube is slightly higher than that of the base fluid (water) with a radius of 0–0.0055 m. Moreover, the solid-phase (graphite) turbulent kinetic energy near the tube wall with a radius of 0.0055–0.006 m gradually increases by about 17 times, and 10 times the turbulent kinetic energy of the water at particle sizes of 1 μm and 5 μm , respectively. Near the tube wall, the addition of microparticles increases the turbulent kinetic energy due to the irregular movement of microparticle suspensions, which does not only effectively enhance the disturbance of the boundary layer but destroys the effect of the conductive boundary layer. The enhancement of the particle size of 1 μm is higher than that at 5 μm due to the number of microparticles in the same volume fraction. In Figure 14, the interphase heat transfer coefficient of the graphite microfluid for a particle size of 1 μm is about 5 times that of a particle size of 5 μm . The reason for this is that a smaller particle size indicates a larger contact surface area for the heat transfer. In the same volume, the number of particles with a size of 1 μm is 125 times that of 5 μm in size, and the surface area is 5 times larger. As shown in Figure 15, the temperature in the middle cross-section of the tube is higher than that of the water, because the increase of the equivalent thermal conductivity of the microfluid and the turbulent kinetic energy improves the heat transfer by adding the microparticles with good thermal conductivity. The greater the volume fraction of the microparticle, the greater the temperature change.

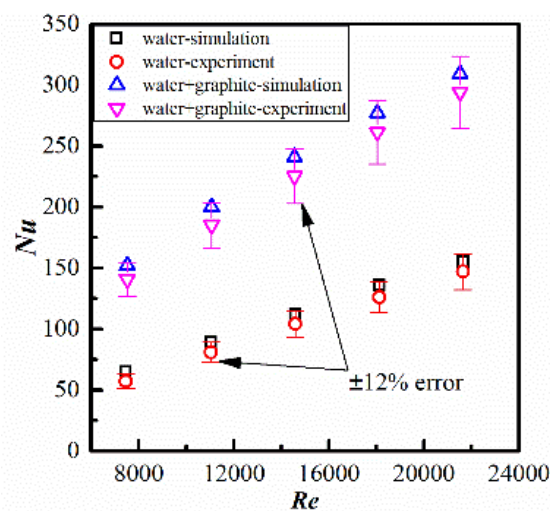


Figure 12. Comparison of the simulation and experiment.

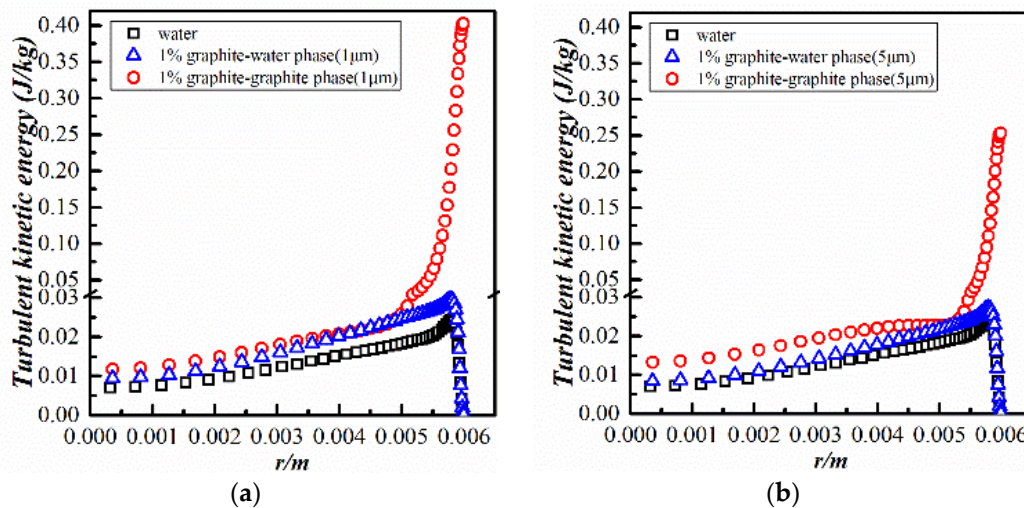


Figure 13. The turbulent kinetic energy in the middle cross-section of the tube at $Re = 23,000$: (a) a graphite particle size of $1\ \mu\text{m}$ with a volume fraction of 1.0%; (b) a graphite particle size of $5\ \mu\text{m}$ with a volume fraction of 1.0%.

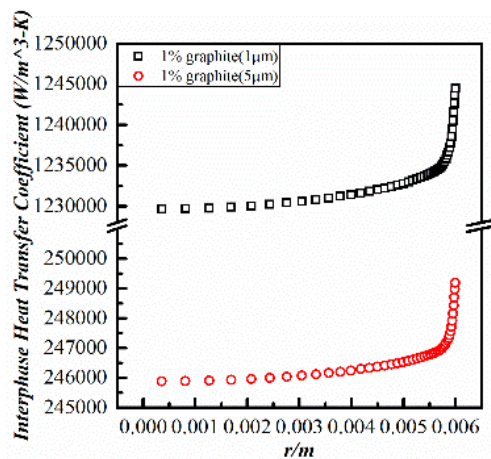


Figure 14. The interphase heat transfer coefficient in the middle cross-section of the tube at $Re = 23,000$.

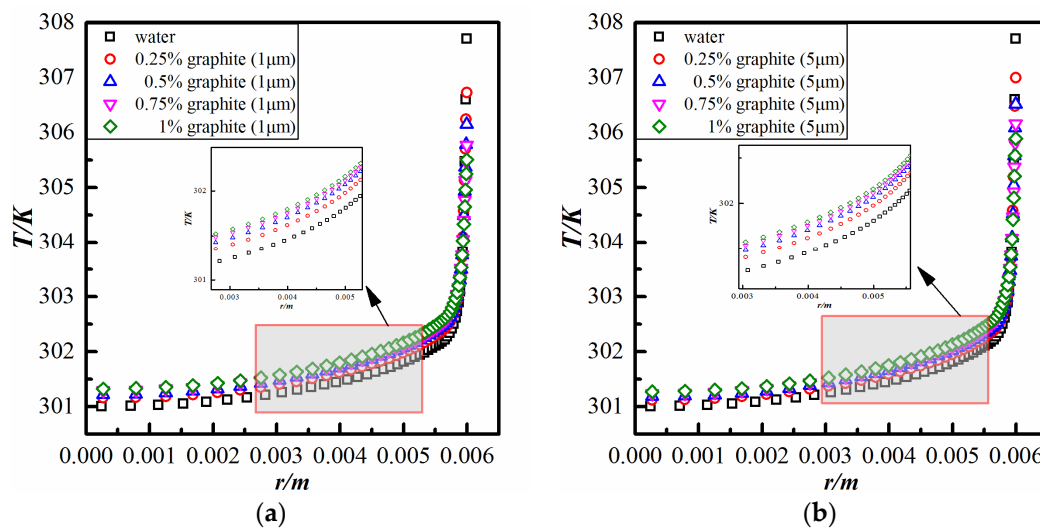


Figure 15. The temperature in the middle cross-section of the tube at $Re = 23,000$: (a) a graphite particle size of $1\ \mu\text{m}$; (b) a graphite particle size of $5\ \mu\text{m}$.

In general, the turbulent convective heat transfer enhancement of microfluid flow is mainly due to two aspects, i.e., the increase in turbulent kinetic energy due to the irregular movement of the microparticle suspensions and the increased equivalent thermal conductivity and interphase heat transfer by adding microparticles with higher thermal conductivity, as illustrated in Equation (3).

4. Conclusions

The results of this study indicate the feasibility of convection heat transfer enhancement by using microparticle multiphase flow for turbulent flow in a tube, based on the Nusselt number, friction factor and thermal performance characteristics of graphite, Al₂O₃ and CuO microfluid, with a particle volume fraction of 0.25%–1.0% and a Reynolds number ranging from 7000 to 23,000. The conclusions can be drawn as follows:

- (1) A variety of microfluids (Graphite, Al₂O₃ and CuO) were studied in a vertical tube. The results show that the heat transfer performance of the various microfluids is better than that of water. The graphite microfluid provides the best thermal performance compared to the other two microparticle suspensions. All the microfluids enhanced heat transfer but increased flow resistance.
- (2) Both graphite microfluids (those with 5 µm and 1 µm graphite particles) further show that the microfluid with 1 µm particles experiences higher heat transfer enhancement than that with 5 µm particles. It is concluded that the smaller the size of particles, the stronger the heat transfer effect and the more significant the friction loss.
- (3) The regression equations obtained in the present paper provide the correlative coefficient of the Nusselt number and the friction factor. The predicted results are in good agreement with the experimental results within a deviation of ± 10% and ± 5% for the Nusselt number and friction factor, respectively.
- (4) The simulation results using the Eulerian–Eulerian granular flow model and considering the microparticle suspension as a continuum show that an increase in the equivalent thermal conductivity of the microfluid and an increase in the turbulent kinetic energy near the wall are two key factors that enhance turbulent convective heat transfer.

Author Contributions: Conceptualization, T.W. and Z.G.; methodology, T.W. and Z.G.; validation, T.W., Z.G. and W.J.; investigation, T.W.; data curation, T.W.; writing—original draft preparation, T.W.; writing—review and editing, T.W., Z.G. and W.J.; supervision, Z.G. and W.J.; funding acquisition, T.W. All authors have read and agreed to the published version of the manuscript.

Funding: This research was funded by the Program of Science and Technology Development Projects of Zhejiang Province, grant number 2015C31133.

Conflicts of Interest: The authors declare no conflict of interest.

Nomenclature

A	heat transfer surface area (m ²)
c_p	specific heat capacity of fluid (J/kg·K)
d	diameter of the tube (m)
f	friction factor
h	heat transfer coefficient (W/m ² ·K)
k	thermal conductivity (W/m·K)
L	length of the test section (m)
m	mass flow rate (kg/s)
Nu	Nusselt number
ΔP	pressure drop (Pa)
Q	heat transfer rate (W)

Re	Reynolds number
T	temperature (K)
V	mean axial flow velocity (m/s)
K	overall heat transfer coefficient ($W/m^2 \cdot K$)
ϕ	volume fraction of microparticle (%)
ρ	density (kg/m^3)
μ	fluid dynamic viscosity (Pa·s)
η	thermal performance factor
Greek symbols	
c	cold fluid
h	hot fluid
i	inner
o	outer
w	water
mf	microfluid
mp	microparticle
in	inlet
out	outlet

References

- Hajmohammadi, M.R.; Maleki, H.; Lorenzini, G.; Nourazar, S.S. Effects of Cu and Ag nano-particles on flow and heat transfer from permeable surfaces. *Adv. Powder Technol.* **2015**, *26*, 193–199. [[CrossRef](#)]
- Zhu, H.; Zhang, C.; Liu, S.; Tang, Y.; Yin, Y. Effects of nanoparticles clustering and alignment on thermal conductivities of Fe_3O_4 aqueous nanofluids. *Appl. Phys. Lett.* **2006**, *89*, 1–3. [[CrossRef](#)]
- Vajjha, R.S.; Das, D.K.; Namburu, P.K. Numerical study of fluid dynamic and heat transfer performance of Al_2O_3 and CuO nanofluids in the flat tubes of a radiator. *Int. J. Heat Fluid Flow* **2010**, *31*, 613–621. [[CrossRef](#)]
- Demir, H.; Dalkilic, A.S.; Kürekci, N.A. Numerical investigation on the single phase forced convection heat transfer characteristics of TiO_2 nanofluids in a double-tube counter flow heat exchanger. *Int. Commun. Heat Mass Transf.* **2011**, *38*, 218–228. [[CrossRef](#)]
- Utomo, A.T.; Haghighi, E.B. The effect of nanoparticles on laminar heat transfer in a horizontal tube. *Int. J. Heat Mass Transf.* **2014**, *69*, 77–91. [[CrossRef](#)]
- Takabi, B.; Shokouhmand, H. Effects of Al_2O_3 -Cu/water hybrid nanofluid on heat transfer and flow characteristics in turbulent regime. *Int. J. Mod. Phys. C* **2015**, *26*, 15–47. [[CrossRef](#)]
- Takabi, B.; Gheitaghy, A.M.; Tazraei, P. Hybrid water-based suspension of Al_2O_3 and Cu nanoparticles on laminar convection effectiveness. *J. Thermophys. Heat Transf.* **2016**, *30*, 523–532. [[CrossRef](#)]
- Azmi, W.H.; Abdul, H.K.; Mamat, R.; Sharma, K.V.; Mohamad, M.S. Effects of working temperature on thermo-physical properties and forced convection heat transfer of TiO_2 nanofluids in water-Ethylene glycol mixture. *Appl. Therm. Eng.* **2016**, *106*, 1190–1199. [[CrossRef](#)]
- Sun, D.; Yang, D. Experimental study on the heat transfer characteristics of nanorefrigerants in an internal thread copper tube. *Int. J. Heat Mass Transf.* **2013**, *64*, 559–566. [[CrossRef](#)]
- Yang, S.; Zhang, L.; Xu, H. Experimental study on convective heat transfer and flow resistance characteristics of water flow in twisted elliptical tubes. *Appl. Therm. Eng.* **2011**, *31*, 2981–2991. [[CrossRef](#)]
- Tang, X.; Dai, X.; Zhu, D. Experimental and numerical investigation of convective heat transfer and fluid flow in twisted spiral tube. *Int. J. Heat Mass Transf.* **2015**, *90*, 523–541. [[CrossRef](#)]
- Bhadouriya, R.; Agrawal, A.; Prabhu, S.V. Experimental and numerical study of fluid flow and heat transfer in a twisted square duct. *Int. J. Heat Mass Transf.* **2015**, *82*, 143–158. [[CrossRef](#)]
- Pal, S.; Saha, S.K. Laminar fluid flow and heat transfer through a circular tube having spiral ribs and twisted tapes. *Exp. Therm. Fluid Sci.* **2015**, *60*, 173–181. [[CrossRef](#)]
- Wongcharee, K.; Eiamsa-ard, S. Heat transfer enhancement by using CuO/water nanofluid in corrugated tube equipped with twisted tape. *Int. Commun. Heat Mass Transf.* **2012**, *39*, 251–257. [[CrossRef](#)]

15. Sun, B.; Yang, A.; Yang, D. Experimental study on the heat transfer and flow characteristics of nanofluids in the built-in twisted belt external thread tubes. *Int. J. Heat Mass Transf.* **2017**, *95*, 712–722. [[CrossRef](#)]
16. Buzea, C.; Pacheco, I.I.; Robbie, K. Nanomaterials and nanoparticles: sources and toxicity. *Biointerphases* **2007**, *2*, MR17–MR71. [[CrossRef](#)]
17. Tae-Hyun, C.; Kwon-Soo, L.; Chang-Hoan, L. An experimental study on velocity and temperature of Al/water microfluid in a circular tube with swirl. *J. Vis.* **2014**, *17*, 59–68.
18. Zhu, J.Y.; Tang, S.; Pyshar, Y.; Thomas, B.; Khoshmanesh, K.; Ghorbani, K. Enhancement of laminar convective heat transfer using microparticle suspensions. *Heat Mass Transf.* **2017**, *53*, 169–176. [[CrossRef](#)]
19. Wang, T.; Jin, W.; Gao, Z.; Xiao, J.; Tao, W.; Tang, J. Turbulent flow and enhanced heat transfer induced by Cu-water microfluid in tube. *J. Vib. Shock* **2018**, *37*, 108–114. [[CrossRef](#)]
20. Stokes, G.G. On the Effect of the Internal Friction of Fluids on the Motion of Pendulums. *Trans. Camb. Philo. Soc.* **1851**, *9*, 89–106.
21. Moffat, R.J. Describing the uncertainties in experimental results. *Exp. Fluid Therm.* **1988**, *1*, 3–17. [[CrossRef](#)]
22. Maxwell, J.C. *Treatise on Electricity and Magnetism*; Dover: New York, NY, USA, 1954.
23. Einstein, A. Berichtigung, zu, meiner, Arbeit. eine neue Bestimmung der Molekul-dimensionen. *Ann. Phys.* **1911**, *34*, 591. [[CrossRef](#)]
24. Wilson, E.E. A basis of rational design of heat transfer apparatus. *ASME J. Heat Transf.* **1915**, *37*, 47–70.
25. Gidaspow, D. *Multiphase Flow and Fluidization*; Academic Press: Boston, MA, USA, 1994.
26. Wen, C.Y.; Yu, Y.H. Mechanics of Fluidization. *Chem. Eng. Prog. Symp. Ser.* **1966**, *62*, 100–111.
27. Ergun, S. Fluid Flow through Packed Columns. *Chem. Eng. Prog.* **1952**, *48*, 89–94.
28. Schmidt, A.; Renz, U. Numerical Prediction of Heat Transfer in Fluidized Beds by a Kinetic Theory of Granular Flows. *Int. J. Therm.* **2000**, *39*, 871–885. [[CrossRef](#)]
29. Martinek, J.; Ma, Z. Granular Flow and Heat-Transfer Study in a Near-Blackbody Enclosed Particle Receiver. *J. Sol. Energy Eng.* **2015**, *137*, 1–9. [[CrossRef](#)]
30. White, F.M. *Viscous Fluid Flow*; McGraw-Hill: New York, NY, USA, 2005.
31. Bayat, J.; Nikseresht, A.H. Thermal performance and pressure drop analysis of nanofluids in turbulent forced convective flows. *Int. J. Therm. Sci.* **2012**, *60*, 236–243. [[CrossRef](#)]
32. Gnielinski, V. New equations for heat and mass-transfer in turbulent pipe and channel flow. *Int. Chem. Eng.* **1976**, *16*, 359–368.



© 2020 by the authors. Licensee MDPI, Basel, Switzerland. This article is an open access article distributed under the terms and conditions of the Creative Commons Attribution (CC BY) license (<http://creativecommons.org/licenses/by/4.0/>).